Zhao, Guomin; Huang, Yanping; Mei, Changtong; Zhai, Shengcheng; Xuan, Yan; Liu, Zhipeng; Pan, Mingzhu; Rojas, Orlando J.

Chiral Nematic Coatings Based on Cellulose Nanocrystals as a Multiplexing Platform for Humidity Sensing and Dual Anticounterfeiting

Published in:
Small

DOI:
10.1002/smll.202103936

Published: 16/12/2021

Document Version
Publisher's PDF, also known as Version of record

NANO · MICRO small
www.small-journal.com

Chiral Nematic Coatings Based on Cellulose Nanocrystals as a Multiplexing Platform for Humidity Sensing and Dual Anticounterfeiting

Guomin Zhao, Yanping Huang, Changtong Mei, Shengcheng Zhai, Yan Xuan, Zhipeng Liu, Mingzhu Pan,* and Orlando J. Rojas**

The need for a precise regulation of the properties of chiral nematic structures in response to external stimuli is addressed. Self-assembled iridescent coatings are produced under the effect of electrostatic interactions between cellulose nanocrystals and poly(acrylic acid), endowing a high anisotropic dissymmetry (>0.3) and sensitivity to environmental humidity (13.1 nm/1% at 68–75% relative humidity, RH). The phenomena associated with shifts in selective light reflection (green to orange) and polarization, facilitate tunable transmitted colors (blue to orange) at given rotation angles (RA). Such properties are conveniently integrated into a "RH-RA-color" ternary code that is introduced as an anticounterfeiting technology, taking advantage of multicolor patterns that conveniently track with changes in RH and RA. The proposed charge-driven assembly opens new opportunities for chiral nematic materials that enable precise optical sensing and information encryption.

1. Introduction

Making part of nature's diversity, creatures such as beetles and butterflies display vivid colors as a result of the interactions of sunlight with the chiral hierarchical structure of the respective exoskeletons, which can be adapted in response to functional and survival demands.[1] Inspired by nature, chiral coatings have been applied on smart materials and sensors to trigger a stimuli-responsive behavior, for example, via changes in selective reflection and diffraction according to environmental factors (humidity, heat, stress, electrical current, and pH, among others).[2,3] Examples of such structures include chiral intelligent assemblies that include traditional chiral donors, such as crystalline TiO_2 microspheres,[4] thiol-acrylate chemistries,[5] and semiinterpenetrating polymer networks.[6] Unfortunately, most of the reported chiral nanostructures are inefficient in translating changes in chiral nematic structure into readable signals. Hence, there is a major need to develop chiral donors that are suitable as intelligent coatings while being easy to control or regulate.

Cellulose nanocrystal (CNC) self-assembles into chiral nematic organizations upon evaporation-induced self-assembly (EISA), forming layers that display periodic spiral structures arranged along a given axis.[7] The high number density of hydroxyl groups on the surface of the cellulose nanocrystals enables mesoporous structures with adjustable channels and binding sites, depending on the chiral nematic structure.[8] The latter can be tuned by the alternation of the stimuli-induced helical pitch, leading to distinctive color changes. Hence, CNC films and coatings have been used as a scaffold for the construction of humidity-,[9] light-,[10] stress-,[11] magnetic-responsive materials.[12] The tunable helical pitch is highly dependent on external stimuli but effective implementation of related principles in devices has remained as a major challenge in the area.

Electrostatic interactions have been recognized as critical in chiral constructions and stimuli-responsiveness,[13] relevant to Au nanocluster phosphors,[14] amino acid aggregators,[15] beta-cyclodextrin pH sensors,[16] information encryption, and L- and D-tryptophan detectors for use with human urine and blood serum. The combination of CNC with neutral polymers, such as poly(ethylene glycol), allows control of the helical pitch as a result of the hydrogen-bonding interactions caused by their

G. Zhao, Y. Huang, C. Mei, S. Zhai, Z. Liu, M. Pan
College of Materials Science and Engineering
Co-Innovation Center of Efficient Processing and Utilization of Forest Resources
Nanjing Forestry University
Nanjing 210037, China
E-mail: zpliu@njfu.edu.cn; mzpan@njfu.edu.cn

G. Zhao, O. J. Rojas
Bioproducts Institute
Department of Chemical and Biological Engineering
Department of Chemistry and Department of Wood Science
University of British Columbia
Vancouver, BC V6T 1Z3, Canada
E-mail: orlando.rojas@ubc.ca

Y. Xuan
Analysis and Testing Center of Nanjing Forestry University
Nanjing 210037, China

O. J. Rojas
Department of Bioproducts and Biosystems
School of Chemical Engineering
Aalto University
Aalto 00076, Finland

The ORCID identification number(s) for the author(s) of this article can be found under https://doi.org/10.1002/smll.202103936.

DOI: 10.1002/smll.202103936

similar mesogenic moieties that carry hydroxyl groups. The role of electrostatic interactions in related applications has not been fully recognized.[17] CNC/waterborne polyurethane (PU) composites displaying instant optical response to water and gas have been reported[18] but, to the best of our knowledge, no reports exist on the use of electrostatic interactions to achieve precise chiral constructions that act as stimuli-response coatings.

Polyelectrolytes, or ionizable polymers possessing cationic or anionic charges along the polymer chain,[19] might enable conformational changes to produce the helical structure. Meanwhile, the polymer backbone can have a positive influence on the mechanical properties of composite materials. Taking advantage of the properties of polyelectrolytes, we envision that their self-assembly with CNC, for example, via electrostatic interactions, will enable a fine regulation to the helical pitch. The interactions between CNCs and polyelectrolytes are dependent on the charge density of both species and, also, on the polymer conformation and network formation. Such effects also govern the assembly process and regulate the helical pitch.[20] Moreover, electrostatic interactions can be influenced by the stimuli, such as humidity,[21] pH,[22] ion type and concentration,[23] which are factors that can be considered in the development of intelligent coatings.

We introduce an efficient strategy to self-assemble chiral humidity-responsive coatings via electrostatic interactions between CNC and polyacrylic acid (PAA). The electrostatic repulsion between CNC and PAA dominates the transfer of chiral structures while their affinity can be used for rapid humidity response. Specially, transmitted colors depend on changes of relative humidity (RH) and rotation angles (RA). These two latter aspects "RH-RA-color" are considered in the construction of ternary anticounterfeiting systems suitable for encrypting information and for humidity sensing.

2. Results

2.1. Evolution of Chiral Conformation

We introduce waterborne PAA as a commercially available and inexpensive anionic polyelectrolyte that fits in the left-handed CNC structure. A CNC/PAA colloidal suspension was prepared by high-energy stirring, and the chirality of the resultant iridescent coatings was found to depend on PAA content (2, 5, 10, 20, and 30 wt%). The range of values of zeta potential of mixtures that include CNC (-34.6 mV) and PAA (-17.9 mV), increases to -37.0 mV (CNC/PAA2) or -45.1 mV (CNC/PAA20), **Figure 1**a. Hence, there is an indication that the respective self-assembly resulted from the electrostatic repulsions between the anionic groups (OSO_3- in CNC and COO− in PAA). At PAA loading of 30 wt%, steric hindrance induces a weakened repulsion between OSO_3- and COO−, which according to Coulomb's law,[24] leads to a reduced value of the zeta potential (-28.6 mV for CNC/PAA30) and facilitates phase separation (Figure 1b, photographs in the inset). We used Na^+ and PU with self-assembled CNC as references. As was the case of CNC/PAA, CNC/Na^+ followed a reduced trend in electrostatic attraction between OSO_3- and Na^+ and resulted in films that were brittle.[25] By contrast, CNC/PU showed a reduced absolute value of zeta potential, indicating weak electrostatic repulsion.

The fingerprint peak of hydroxyl groups in CNC/PAA shifted from 3446 to 3396 cm^{-1}, indicating the formation of hydrogen bonding between the two species (Figure S1, Supporting Information). The crystalline and pore structure that result from self-assembled CNCs are transferred to CNC/PAA systems. As a result, the latter combine the merits of ions and polymers as far as electrostatic repulsion, hydrogen bonding, and steric hindrance that also regulate the shift of color in chiral nematic CNC/PAA during self-assembly (Figure 1b). Meanwhile, noncovalent interactions improve the mechanical properties of CNC/PAA coatings (Figure 1c) and at a PAA content above 10 wt%, the coatings achieve a maximum hardness and adhesion, 6H and level-1, respectively.

The interfacial bonding plays a positive role in the transformation of chiral nematic structures. As expected, the CNC/PAA films formed by EISA exhibited iridescence, corresponding to given chromatic orders, cyan (CNC/PAA2), turquoise (CNC/PAA5), green (CNC/PAA10), and yellow (CNC/PAA20), respectively (Figure 1d and Figure S2a, Supporting Information). The cross-section of the coatings showed a uniform arrangement between CNC and PAA, with periodic spacing and spiral stacking (middle i–iii in Figure 1d). Especially, the CNC/PAA10 coating exhibited an apparent chiral nematic structure, with a pitch of 350 nm. The formed chiral photonic structures (polarized optical microscopy, POM), showed uniform fingerprint textures, typical of chiral nematic order, with a pitch of 361 nm and green pattern, which gradually appeared during the EISA process (right iii in Figure 1d). Additionally, UV–Visible (UV–Vis) and circular dichroism (CD) spectra showed that the maximal reflection wavelength (λ_{max}) peaked in the visible region for the CNC/PAA10 iridescent coatings (Figure 1e). Compared to coatings produced from neat CNC, the λ_{max} of CNC/PAA10 presented a red-shift, both in UV–Vis and CD spectra, likely a result of electrostatic repulsion and steric hindrance. The strong positive signals present in CD spectra indicate a left-handed chiral nematic organization in CNC/PAA.[7a]

The pitch of CNC/PAA iridescent coatings increased gradually with increasing PAA content, from 2 to 20 wt% (Figure 1f and Figure S2b,c, Supporting Information), corresponding to a gradual change in λ_{max} from 430 to 568 nm (Figure S3, Supporting Information). This phenomenon is also influenced by the enhanced electrostatic repulsion and steric hindrance of PAA. However, the chiral nematic helical structure disappears in CNC/PAA30 due to phase separation (Figure S4, Supporting Information).

To reveal the influence of PAA content on the structural color of the iridescent coatings, the UV–Vis absorbance spectra were transformed into Commission on Illumination (CIE) chromaticity values (Figure 1g), corresponding to the iridescent cyan ($x = 0.1710$, $y = 0.0121$, CNC/PAA2), turquoise ($x = 0.1005$, $y = 0.1368$, CNC/PAA5), green ($x = 0.2216$, $y = 0.7501$, CNC/PAA10), and yellow ($x = 0.4340$, $y = 0.5639$, CNC/PAA20), respectively. The results demonstrate that CNC chiral nematic structures occur in the presence of PAA and are precisely regulated by PAA content. Based on the chirality and mechanical robustness of the CNC/PAA coatings, the CNC/PAA10 system was selected for further tests with such iridescent coatings. For this purpose, the samples were conditioned under variable relative humidity (RH) (Figure S5, Supporting Information).

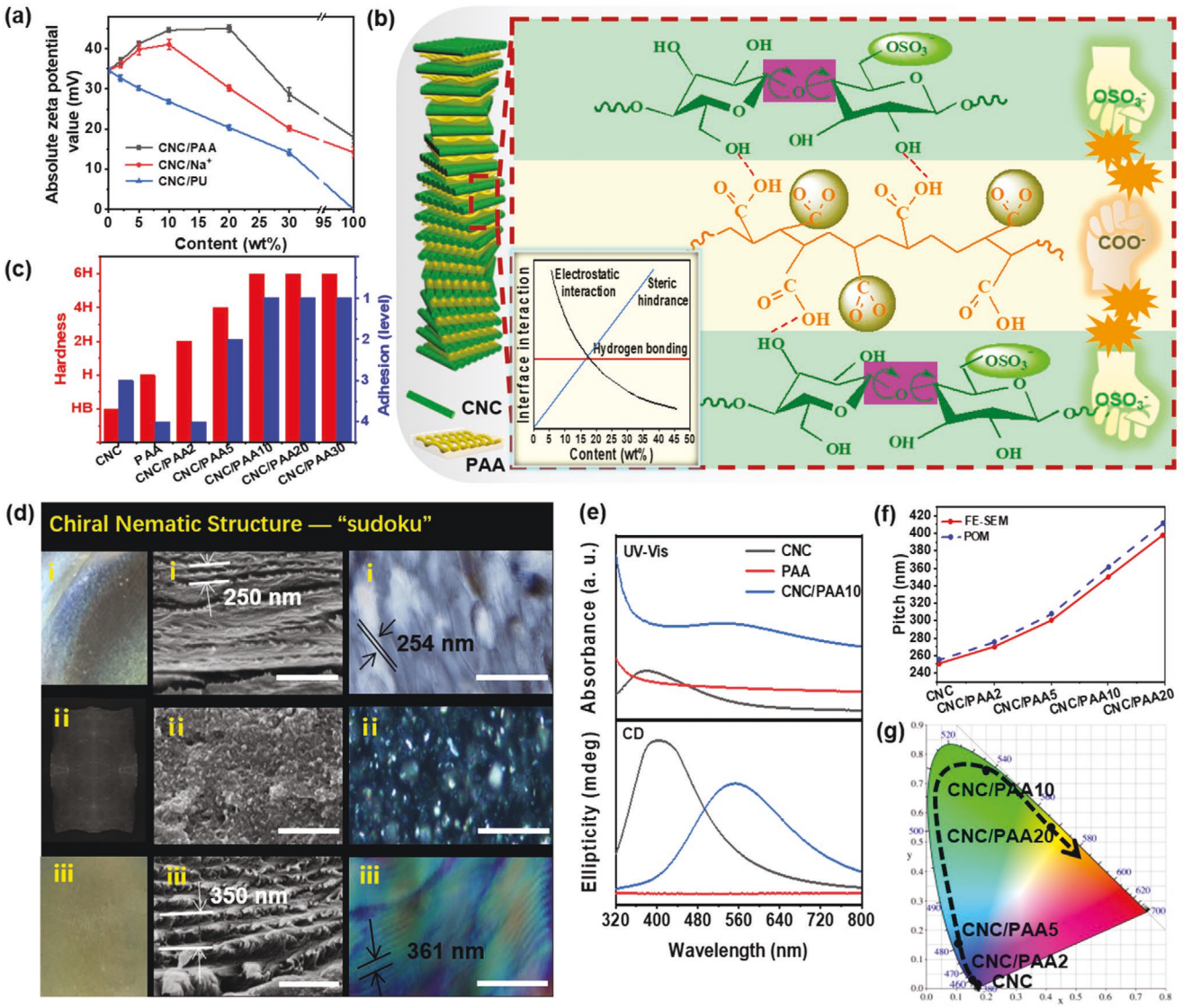

Figure 1. Self-assembly of CNC/PAA iridescent coatings. a) Zeta potential values of CNC/PAA, CNC/Na^+ and CNC/PU as a function of composition. b) Schematic illustration of self-assembled CNC and PAA with left-handed chiral nematic organization. The inset image represents the changes in interfacial interactions between CNC and PAA as a function of composition (electrostatic interaction, hydrogen bonding, and steric hindrance). c) Mechanical properties of CNC/PAA coatings (hardness and adhesion). d) Chiral nematic structure of CNC/PAA iridescent coatings: direct photograph (left), FE-SEM (cross section, middle) and POM (right) images of CNC/PAA coatings formed upon EISA corresponding to CNC (i), PAA (ii), and CNC/PAA10 (iii). The scale bar in FE-SEM and POM images is 1 µm and 2 µm, respectively. e) UV–vis absorbance and CD spectra of CNC/PAA coatings. f) Approximated pitch of CNC/PAA coatings obtained from FE-SEM and POM images. g) CIE chromaticity diagram of CNC/PAA coatings.

2.2. Humidity Response

The CNC/PAA10 iridescent coating show a visible color, tunable with RH. The colors sequentially appear as violet (22% RH), cyan (43% RH), orange (75% RH) and red (99% RH) (**Figure 2**a), corresponding to λ_{max} at 448, 495, 624, and 658 nm, respectively (Figure S6, Supporting Information). The λ_{max} redshift is likely related to the 1) extension of the coating film and expansion of helical pitch upon water absorption, and 2) the increase of average refractive index (n_{avg}) induced by the different refractive indices of water (n = 1.33), CNC (n = 1.54),[7a] and PAA (n = 1.51).[26] Moreover, the absorbance intensity of the peaks is reduced with the increased RH, which is ascribed to a large refraction from water absorption. Notably, this phenomenon is reversible, with a color memory ratio > 97% after 10 cycles (Figure S7, Supporting Information). The spectra of the iridescent coating are transformed to CIE chromaticity values (Figure 2b), which indicate a shift from violet to red, consistent with the color change of the iridescent coating.

The CNC/PAA10 iridescent coating shows a slowly increase in λ_{max} with RH increasing from 22% to 68% (Figure 2c). It is worth noting that a sharp λ_{max} increase occurs as the RH increases from 68% to 75%. However, the growth in λ_{max} becomes less marked as RH reaches 99%. To quantify the

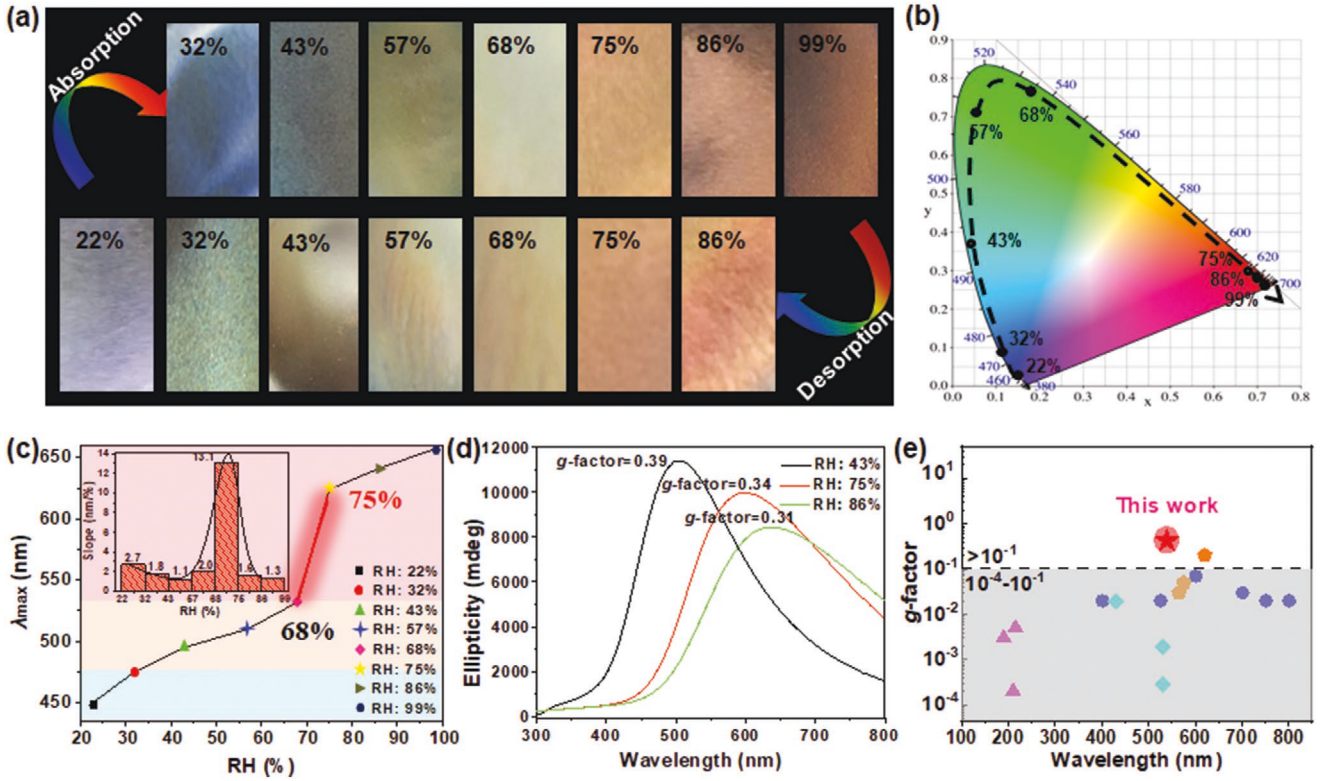

Figure 2. Humidity response of CNC/PAA10 iridescent coatings. a) Photographs of CNC/PAA10 exposed to air at different relative humidity, as indicated, and showing different colors, according to water absorption (top) and desorption (bottom) processes. b) CIE chromaticity diagram. c) λ_{max} of the iridescent coating at given RH The inset photograph represents the slope of λ_{max} as function of RH. d) CD spectra. e) g-factor and comparison with various chiral structures.

humidity response rate, we used the slope of λ_{max} as a function of RH (inset of Figure 2c). A RH change from 22% to 68%, results in a slope that remains fairly unchanged (2–2.7 nm/1% range). Notably, the slope sharply increases to 13 nm/1% as the RH increases from 68% to 75%. It then decreases to <2 nm/1% as RH approaches 99%. Accordingly, the CNC/PAA iridescent films display less significant color differences in the %RH range between 22% and 68% RH, going from violet to green. The change is more noticeable above 75% RH, going from orange to red (Figure 2a). A "parabolic" change in slope and two distinct color regions at a critical 75% RH reveal the hygroscopic hysteresis behavior in the humidity-response process of CNC/PAA coatings, which is consistent with that of natural wood.[27]

The humidity response of the iridescent coatings relates to the chirality of the CNC/PAA10 coating. CNC/PAA10 at 43%, 75%, and 86% RH produce a strong positive CD signal (Figure 2d), confirming the retention of the left-handed chiral nematic structure. Moreover, as the RH increases from 43% to 86%, the CD peak shifts from 495 nm to 640 nm, owing to an increased n_{avg}. Subsequently, the Kuhn's dissymmetry factor (g-factor) is 0.39 at 43% RH and it slightly decreases at higher humidity, 0.34 (75% RH) and 0.31 (86% RH). Notably, the g-factor of CNC/PAA iridescent coating is greater than that of various chiral structures measured at given RH (Figure 2e and Table S1, Supporting Information), which highlights the potential of the chiral coatings for humidity response and anticounterfeiting.

2.3. Humidity-Response Mechanism

To understand the humidity-response behavior of CNC/PAA10 coating, we measured the mass change of CNC/PAA10 coating, e.g., to probe the humidity-response during water absorption and desorption (22–99% RH range). The swelling profile shows two distinctive stages, **Figure 3**a. At RH < 75%, the films display hysteretic and limited humidity-responsiveness. At RH > 75%, the films gain a substantial mass. The hygroscopic hysteresis of the CNC/PAA10 coating abruptly appears at a critical RH of 75%. We further investigated the relaxation spectra in low-field nuclear magnetic resonance (LF-NMR), e.g., to understand the response behavior of water molecules within the CNC/PAA10 coating. CNC/PAA10 shows T_{21} peaks at RH = 22% and 32% (Figure 3b), assigned to bonded water in the crystallization regions, adsorbed via electrostatic attractions and hydrogen bonding.[28] At increased RH, 43%, 57%, and 68%, CNC/PAA10 not only exhibits a T_{21} peak, but also a new T_{22} peak, which is attributed to water weakly bound to the amorphous regions. Notably, another new T_{23} peak is observed (enlarged in the relaxation spectra of Figure 3c) as the RH increases to 75%, 86%, and 99%, corresponding to free water, mainly adsorbed in the pores of the iridescent coating by van der Waals forces. The hydrogen bonding between CNC, PAA, and water molecules is also confirmed by FTIR spectroscopy (Figure S8, Supporting Information), which increases with RH.

The three bonding states of water molecules indicate a multistage humidity response (Figure 3d. At lower RH (22–32%),

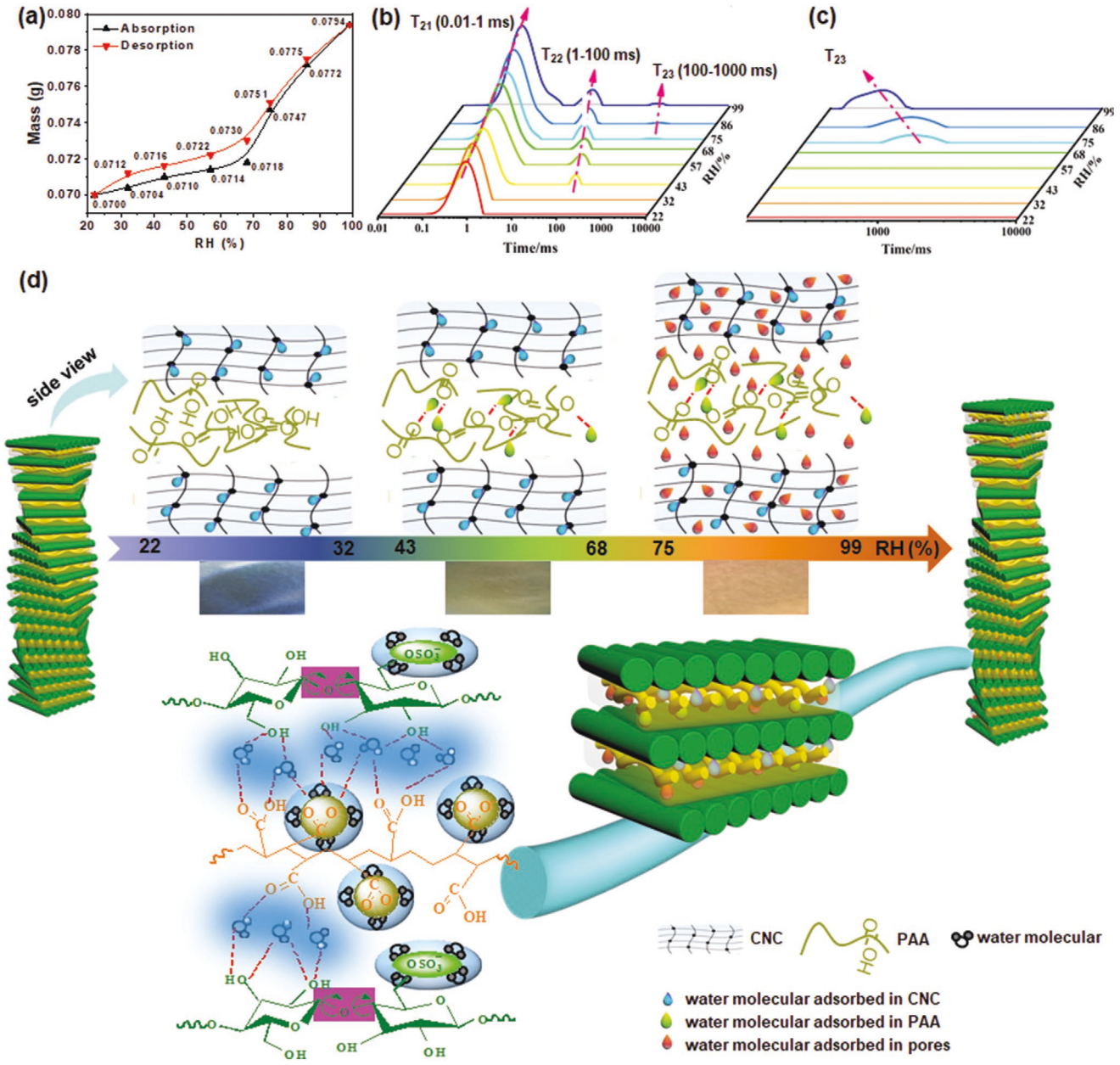

Figure 3. Mechanism of humidity response of CNC/PAA10 iridescent coatings. a) Mass change during water absorption and desorption at given RH. b,c) Relaxation spectra of LF-NMR in a RH gradient at 0.01–10000 ms and 100–1000 ms, respectively. d) Schematic illustration of the mechanism of humidity response of CNC/PAA10 iridescent coatings.

absorption of water molecules takes via hydroxyl group present in the crystalline regions, consistent with a Langmuir-type sorption.[29] At moderate RH levels (43–68%), water molecules couple with hydroxyl groups in the crystalline and amorphous regions, in a Langmuir-type sorption isotherm. In these two stages, water molecules are physically absorbed, resulting in a small volume expansion and less distinguishable color differences. At higher RH levels (75–99%), besides the Langmuir-type sorption, water molecules are randomly absorbed in the pores of CNC/PAA10, which is in accordance with Henry's law-type random sorption.[29] The increase of sites for water absorption as well as film swelling, leads to changes in the visible color. Consequently, a Langmuir- and Henry's law-type random and multistage water sorption occur in CNC/PAA10. In addition, a significant redshift (λ_{max} and iridescent color) occurs at a critical RH (75%).

2.4. Anticounterfeiting

Owing to the excellent humidity-responsiveness and large g-factor of CNC/PAA coatings, we next discuss the polarization together with the change in color at given RH levels (**Figure 4**a and Figure S9, Supporting Information). As expected, the CNC chiral nematic structure enables gradual tuning of the transmitted

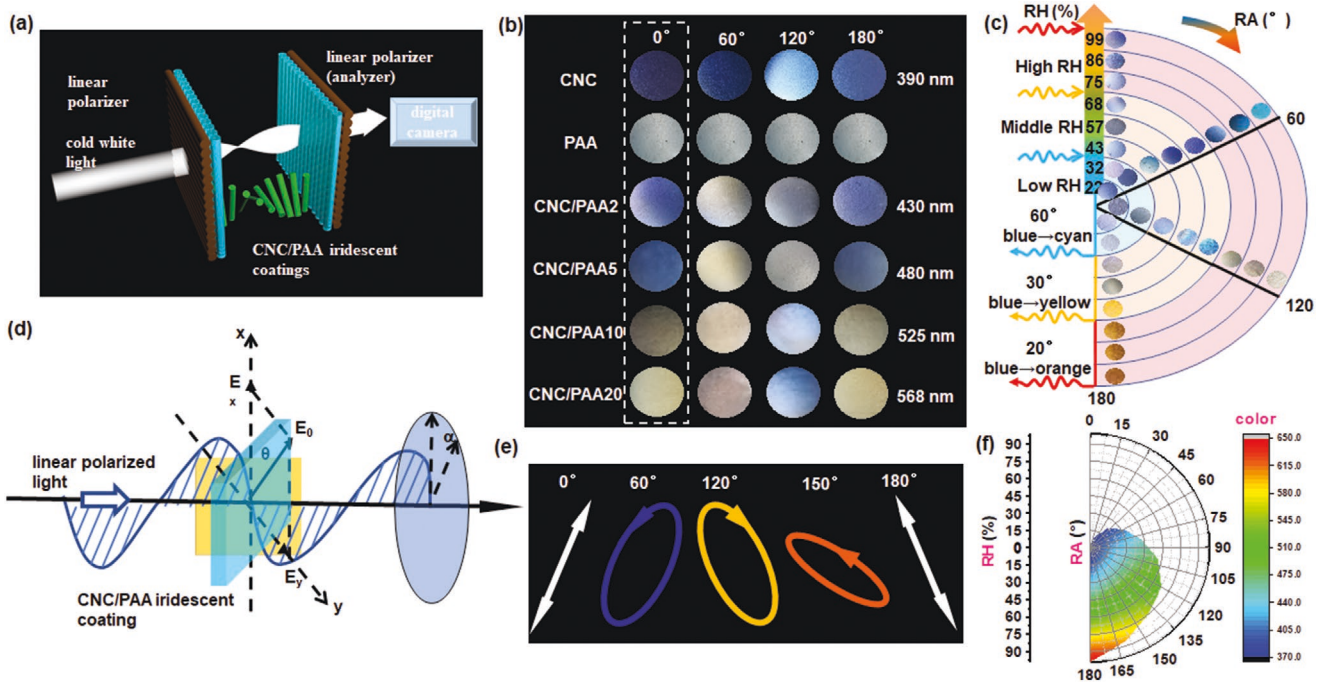

Figure 4. Anticounterfeiting properties of CNC/PAA iridescent coating. a) Schematic illustration of the experimental setup used to measure the transmitted colors. b) Polarization-resolved colors of light transmitted by the iridescent coatings. c) Polarization-resolved colors of light transmitted by CNC/PAA10 under given RHs and RA (every 60°). d) Anticounterfeiting mechanism. e) The vibration track for RA of 0°, 60°, 120°, 150°, and 180° at a 75% RH. f) A "RH-RA-color" ternary anti-counterfeiting code system.

(cross-polarized) colors. By contrast, the color of neat PAA remains unchanged due to its achiral structure. Notably, the CNC/PAA iridescent coating exhibits a color transition under cross-polarized conditions, which further confirms the transition of the chiral nematic structure of CNC to CNC/PAA (0°, dotted box in Figure 4b). The CNC/PAA10 coating shows a dynamic color shift that is cyclic when the analyzer is rotated by 180° during a full rotation (0–360°) (Figure S10, Supporting Information). Especially, the transmitted colors' transfer range (light blue to khaki) of CNC/PAA10 is wider than that of CNC (violet to cyan).

As discussed, the chirality of iridescent coating can be finely tuned by RH. Hence, CNC/PAA10 coatings are further exposed to different RH. Interestingly, the transmitted color of the iridescent film exhibit significant changes with both RH and RA (Figure 4c and Figure S11, Supporting Information). At a 75% RH, the total response changes in terms of transmitted color from blue (0°) to orange (180°). Subtly, the transmitted color shifts from light cyan (20°) to dark gray cyan (40°), easily seen by the naked eye. As the RA is changed to 60°, the transmitted color shifted to blue. Thereafter, the transmission colors of the iridescent film significantly change every 20° during a full rotation. At the other given RH levels, the transmission color is also shifted with RA. However, the response range and efficiency with RA are smaller than that at 75% RH, which is ascribed to the limited humidity-responsiveness of the iridescent coating.

A typical birefringent material has one optical axis, and the anisotropic refractive index (n) of the material can be decomposed into a parallel ($n_{\parallel}$) and cross ($n_{\perp}$) component (generally, $\Delta n = n_{\parallel} - n_{\perp} > 0$). When light passes an anisotropic material, the two components produce a phase difference (δ), described by Equation (1):[30]

$$\delta = \frac{n_{\parallel} - n_{\perp}}{c} d \tag{1}$$

where, c is the speed of incident light, and d is the thickness of the iridescent coating. With an increased RH, the increase in $n_{\parallel}$ is greater than that of $n_{\perp}$, leading to an increased Δn. d also increases with RH. Doubling Δn and d causes the δ to significantly increase at higher RH levels, which expands the transformation range and speed of the transmitted color.

As linear polarized light is incident on the iridescent coating surface (Figure 4d), the two polarization components, X-axis (E_x), and Y-axis (E_y) directions, can be described by Equations (2) and (3),[30] respectively:

$$E_x = E_0 \cos\theta \tag{2}$$

$$E_y = E_0 \sin\theta \tag{3}$$

where θ represents the angle between the polarization direction of incident light and the direction of CNC/PAA chiral nematic layer (X-axis). As the incident light passes through the iridescent coating, the vibrations of the two components, due to the δ, follow Equations (4) and (5), respectively.

$$E_x = E_0 \cos\theta \sin\left(\omega t - \omega \frac{n_{\parallel}}{c} d\right) \tag{4}$$

$$E_y = E_0 \sin\theta \sin\left(\omega t - \omega \frac{n_{\perp}}{c} d\right) \tag{5}$$

Combining Equations (1), (4), and (5), the synthetic vibration of light passing through the iridescent coating can be described by the following expression.

$$E_x^2 + E_y^2 - 2E_xE_y\cos\delta = \frac{E_0^2}{2}\sin^2\delta \quad (6)$$

when the light passes through the analyzer, the final vibration can be expressed by Equation (7) according to Malus law.[31]

$$E = \frac{E_0^2}{2}\sin^2\delta\cdot\cos^2\alpha \quad (7)$$

where, α represents the angle of rotation of the analyzer, that is the RA mentioned above. As the light travels along the iridescent coating, the δ caused by changes in RH gradually increases, and light vibration also changes with increasing of RA, in the order of straight line, ellipse, circle, ellipse, and straight line. Each ellipse tracks with the transmission color of the iridescent coating, therefore, this can be used to hide information about the same color, e.g., to achieve anticounterfeiting and information encryption. For example, at a 75% RH, the vibration track is a straight line (0°), ellipse (60°), ellipse (120°), ellipse (150°), and a straight line (180°), and then, encryption of blue (60°), yellow (120°), and orange (150°) was realized (Figure 4e).

Hence, a "RH-RA-color" ternary anticounterfeiting code system can be established according to the transmitted color change, caused under cross-polarized conditions by vibrations under RH and RA gradients (Figure 4f). This affords a mechanism for dual anticounterfeiting based on the iridescent coatings.

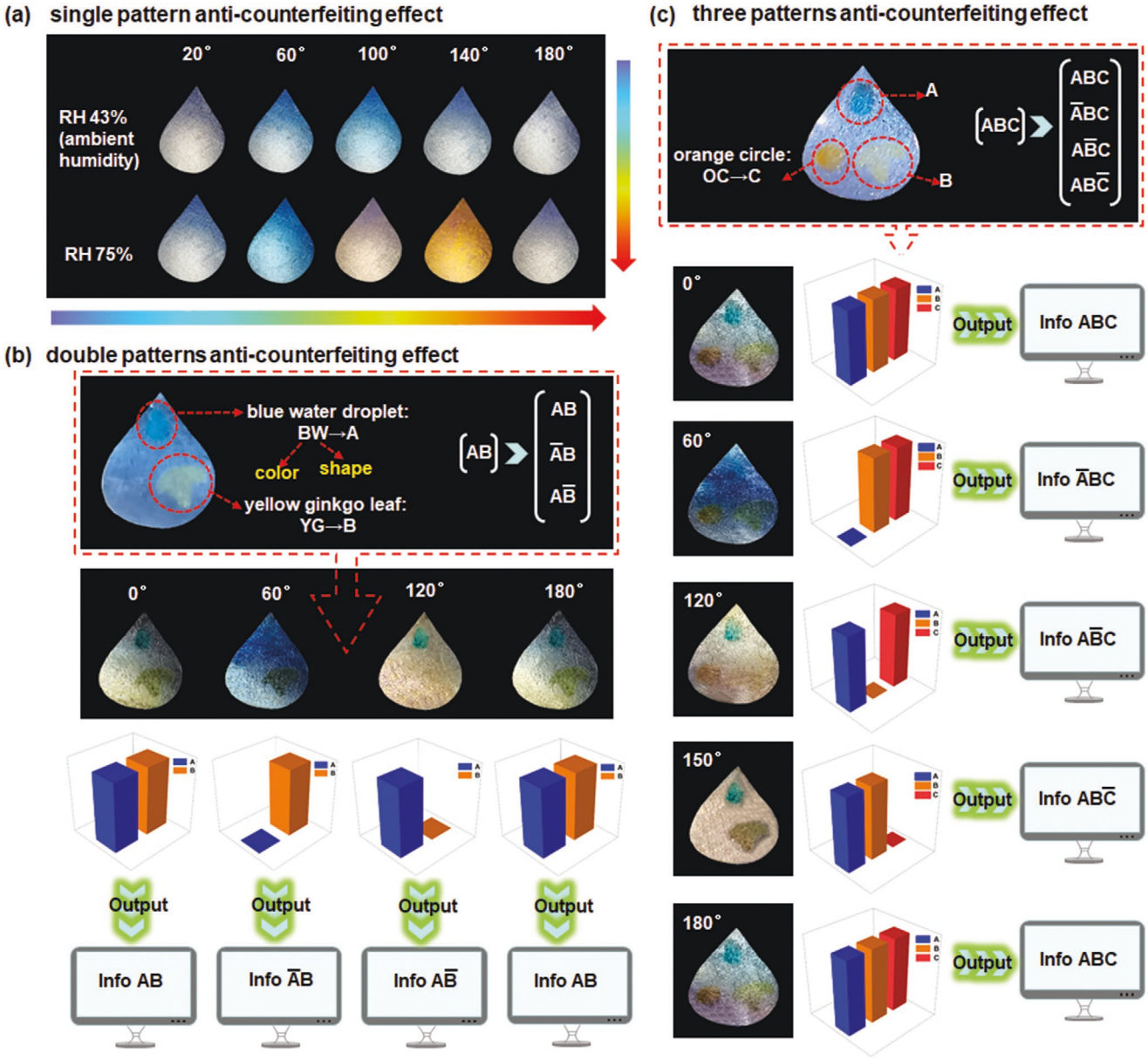

Figure 5. Anticounterfeiting effects of CNC/PAA10 iridescent coating. a) Single pattern anticounterfeiting experiment. b) Double patterns anticounterfeiting effect. c) Three patterns anticounterfeiting result.

To demonstrate the anticounterfeiting effect of the iridescent coatings, several different patterns (single, double, triple) were developed. First, we designed a water droplet of CNC/PAA10 with a single pattern anti-counterfeiting (**Figure 5**a). At a moderate RH of 43%, the color of the patterns first turn to blue, then to light orange, as the RA changes from 0° to 180°. Conversely, at a higher RH, 75%, the more sensitive, clear blue or orange patterns appear at the same RA. Second, we designed a blue water droplets and yellow ginkgo leaf with CNC/PAA10, e.g., to explore the double pattern anti-counterfeiting effect, based on the more vivid color change at a critical 75% RH (Figure 5b). Initially, the blue water droplet (BW→A) and yellow ginkgo leaf (YG→B) were visible, which is encoded as information AB (Info AB). When the analyzer rotates from 0° to 60°, the color changes to blue and covers BW. Thus, the BW disappears and only leaves YG, which is encoded as Info $\overline{A}$B. As the RA continues to 120°, the color overlaps YG, only leaving BW. This opposite vision is encoded as Info A$\overline{B}$. With increasing RA to 180°, BW and YG are both visible again, which is also encoded as Info AB. We further designed blue water droplets (A), yellow ginkgo leaf (B), and orange circle (OC→C) patterns with the CNC/PAA10 coating. At a 75% RH, the three patterns alternately appear and disappear in the version with increasing RA. As RA rotates to 0°, 60°, 120°, 150°, and 180°, the patterns are encoded as Info ABC, Info $\overline{A}$BC, Info A$\overline{B}$C, Info AB$\overline{C}$, and Info ABC, respectively (Figure 5c). Conversely, the encrypted information is deduced according to the encoding. The dynamic appearance and disappearance of these patterns demonstrate that the iridescent coating can be used for three patterns or even multipattern anticounterfeiting and encryption. Current anticounterfeiting systems are mostly based on fluorescence, however, there is a risk of migration and leakage of the fluorescent agent, which is crucial for detection stability and safety during use. Here, the structural color anticounterfeiting is proposed as an environmental-friendly, stable alternative that is stable under environmental factors, making it safer and more reliable. The iridescent coatings afford storage of information and encoding capabilities across a wide color range (blue to orange), with a total number of codes that are considered when combining colors and patterns.

3. Conclusion

A scalable strategy is used to design iridescent coatings with humidity-responsiveness, involving electrostatic interactions between structurally assembled CNC and PAA polyanion. Using a weight ratio of 90:10 (CNC:PAA), the obtained iridescent coating inherits the chiral nematic structure of CNC while being mechanically robust. The CNC/PAA iridescent coating exhibits a visible color shift (green to orange), corresponding to a response range of 92 nm, with an increase of RH from 68% to 75%. Remarkably, the humidity-response of the iridescent coating presents hygroscopic hysteresis behavior due to the multi-stage water uptake that occurs by the effects of constructive physical cross-linking via hydrogen and electrostatic bonding, enabling a sharp shift at a critical RH of 75%. The CNC/PAA iridescent coating shows transmitted colors under cross-polarized conditions, which involves chiral helix structure's polarization, offering an opportunity to develop dual anti-counterfeiting patterns at variable RH. Accordingly, a ternary anticounterfeiting code system is established by the combination "RH-RA-color," which is beneficial for multipattern anticounterfeiting and encryption (e.g., encoding dynamic appearance and disappearance of patterns caused by the changes of RH and RA). We foresee polyelectrolytes to enable a precise helical structure for humidity-responsive iridescent coatings. The proposed CNC/PAA iridescent coating represents a low-cost, stable, and ecofriendly option for optical sensors and multifunctional encryption.

4. Experimental Section

Materials: Waterborne PAA with acrylic resin as the main component (42 wt% solid content) was supplied by Tikkurila Oyj (Vantaa). Microcrystalline cellulose (MCC) power (≈50 µm diameter) was kindly provided by Shanhe Pharmaceutical Excipients Co., Ltd. (Anhui, China). H_2SO_4 (95-98%), potassium acetate ($C_2H_3KO_2$ ≥ 92.0%), magnesium chloride hexahydrate ($MgCl_2 \cdot 6H_2O$ ≥ 98.0%), anhydrous potassium carbonate (K_2CO_3 ≥ 99.0%), sodium bromide (NaBr ≥ 99.0%), potassium iodide (KI ≥ 99.0%), sodium chloride (NaCl ≥ 99.5%), and potassium chloride (KCl ≥ 99.5%, analytical grade) were obtained from Sinopharm Chemical Reagent Co., Ltd. (Nanjing, China). All chemical agents were used without further purification.

Preparation of CNC/PAA Iridescent Coatings: CNC was prepared according to our previous report.[32] The as-prepared, rod-shaped CNC presented an average length of 266 nm, and a diameter of 16 nm (aspect ratio of 17). The $-OSO_3-$ content of the CNC was 0.46%. The zeta potential of the CNC, -34.6 mV indicated good colloidal stability in aqueous suspension.

Figure S12 (Supporting Information) illustrates the preparation of CNC/PAA coatings. The prepared CNC (2 wt%, 200 g) and waterborne PAA were placed into a rounded bottom flask (500 mL), and then sonicated (250 rpm at 25 °C for 10 min) to obtain a homogeneous suspension. Afterward, the CNC/PAA suspension was deposited on the surface of clean glass (5 mm × 12 mm) and dried for 2 d at ambient conditions to obtain CNC/PAA coating films (thickness of 130–150 µm). The coatings were prepared at 2, 5, 10, 20 and 30 wt% PAA concentration, named as CNC/PAA2, CNC/PAA5, CNC/PAA10, CNC/PAA20 and CNC/PAA30, respectively. During EISA, chiral nematic ordering was noted in the obtained CNC/PAA coating, which displayed the structural color. For comparison, neat CNC and PAA films were also prepared by EISA.

Characterizations: A field-emission scanning electron microscope (FE-SEM, HITACHI S4800, Thermo Scientific, USA) was used to evaluate the morphology of cross-sections of CNC/PAA iridescent coatings. The chiral nematic liquid crystal behaviors of the coatings were observed using POM (BX41, Olympus, Japan). FTIR spectra were recorded by an infrared spectrum instrument (VERTEX 80, Bruker, Germany). N_2 sorption isotherms were measured with ASAP 2020 HD88 system (Micromeritics, USA). The pore volumes and pore size distributions were derived from the desorption branches of isotherms using the Barrett-Joyner-Halenda (BJH) model. The specific surface area Sp ($m^2\ g^{-1}$) was estimated with the BET method. UV–Vis (Lambda 950, PE, USA) spectra were performed to investigate the maximal reflection wavelength of CNC/PAA iridescent coatings. CD spectra were recorded using a CD spectrometer (J-1500, Jasco, Japan). X-ray diffraction (XRD) was performed with an X-ray diffractometer (Ultima IV, Rigaku, Japan). The crystallinity index (Cr*I*) was calculated according to Equation (8):[33]

$$\mathrm{CrI}(\%) = \frac{A_{\mathrm{total}} - A_{\mathrm{am}}}{A_{\mathrm{total}}} \times 100 \tag{8}$$

where A_{total} and A_{am} represent the total area of the diffract gram, and the area of the amorphous peak, respectively.

Mechanical Properties Test: Hardness and adhesion of CNC/PAA iridescent coatings were determined according to National Standards of the People's Republic of China GB/T 6739-2006, and GB/T 1720-2006, respectively, which are technically equivalent to ASTM D3363-2005, and ASTM D3359-2009 standard tests. Six different positions were performed in each sample. All the samples were tested at 25 ± 2 °C.

Detection of Humidity-Responsive Behavior: The humidity responsiveness of CNC/PAA iridescent coating was tested in a testing chamber. Samples were placed in a desiccator, and the RH levels within the desiccator were controlled with oversaturated salt solutions. The given salts were used ($C_2H_3KO_2$, $MgCl_2$, K_2CO_3, NaBr, KI, NaCl, KCl, and H_2O), corresponding to equilibrium RH levels of 22%, 32%, 43%, 57%, 68%, 75%, 86%, and 99%, respectively. The RH within the desiccator was monitored with a calibrated traceable digital hygrometer with 1% resolution and ±5% accuracy (HTC-1, Apuhua, China). Humidity-responsive properties of CNC/PAA iridescent coating were measured by a digital still camera (DSC, COOLPIX B600), UV–vis, analytical balance, and CD. The *g*-factor was calculated from the measured absorbance (A) and CD values (Equation 9).[34]

$$g-\text{factor}=\frac{CD}{32980A} \tag{9}$$

The interaction of water molecules with the CNC/PAA iridescent coating was evaluated by nuclear relaxation measurements by using an LF-NMR analyzer VTMR20-010-T-Analyst (Niumg Electric Corporation, China) and an inversion of a multi-exponential fitting analysis (T-invfit, Niumg) program. The strength of the magnetic field was 0.5 ± 0.05 T. Transverse relaxation (T_2) was measured by using the Carr-Purcell-Meiboom-Gill pulse sequence (CPMG). The response cyclicity ability was conducted on a UV–vis spectrophotometer. Samples were alternately explored at increased and decreased humidity conditions for 10 cycles. During each cycle, the maximal reflection wavelength was named as λ_{max1}, λ_{max2}, ..., λ_{max10}, respectively. The response cyclicity was reflected by the color memory ratio (R), which can be calculated using Equation (10).

$$R=1-\frac{\left|\lambda_{max2}-\lambda_{max1}\right|+\left|\lambda_{max3}-\lambda_{max1}\right|+\cdots+\left|\lambda_{max10}-\lambda_{max1}\right|}{9\lambda_{max1}} \tag{10}$$

Detection of Anticounterfeiting Properties: Photographs were taken with a DSC. Macroscopic color changes in transmitted light were detected by polarization-resolved transmission measurements with an optical configuration consisting of a white-light illumination source, iris, linear polarizer, sample, a linear polarizer (analyzer), and DSC. Samples were placed between two crossed linear polarizers (0° represents cross-polarized conditions), and irradiated with a collimated cold white-light source. The angle of the analyzer was changed from 0° (clockwise) to 360° in a step of 1° from the orthogonal configuration, which enabled different wavelengths of light to propagate, rendering different colors in the transmitted light. By rotating the analyzer, the color transition of the transmitted light was observed and recorded with a DSC.

Supporting Information

Supporting Information is available from the Wiley Online Library or from the author.

Acknowledgements

This study was supported by the Natural Science Foundation of Jiangsu Province, China (Grant No. BK20201384), the Science Fund for Distinguished Young Scholars of Nanjing Forestry University (Grant No. NLJQ2015-02), the National First-class Disciplines (PNFD), and the Postgraduate Research & Practice Innovation Program of Jiangsu Province (SJKY19_0895). O.J.R. and G.Z. acknwoledge the Tri-agency Institutional Programs Secretariat (TIPS) for the Canada Excellence Research Chair initiative (CERC-2018-00006) and the Canada Foundation for Innovation (CFI). O.J.R. is also grateful to the European Research Council (ERC) Horizon 2020 research and innovation programme (BioElCell 788489).

Conflict of Interest

The authors declare no conflict of interest.

Data Availability Statement

Research data are not shared.

Keywords

anticounterfeiting, cellulose nanocrystals, chiral nematic coatings, electrostatic interactions, humidity response

Received: July 6, 2021
Revised: August 19, 2021
Published online:

[1] V. Sharma, M. Crne, J. O. Park, M. Srinivasarao, *Science* **2009**, *325*, 449.

[2] a) Y. Gao, S. S. Pan, G. Y. Guo, Q. Q. Gu, R. H. Pan, Y. J. Guan, J. Hu, *Prog. Org. Coat.* **2020**, *139*, 105452; b) Q. Wu, L. X. Gong, Y. Li, C. F. Cao, L. C. Tang, L. B. Wu, L. Zhao, G. D. Zhang, S. N. Li, J. F. Gao, Y. J. Li, Y. W. Mai, *ACS Nano* **2018**, *12*, 416; c) H. Liu, Q. M. Li, Y. B. Bu, N. Zhang, C. F. Wang, C. F. Pan, L. W. Mi, Z. H. Guo, C. T. Liu, C. Y. Shen, *Nano Energy* **2019**, *66*, 104143; d) N. Herzer, H. Guneysu, D. J. D. Davies, D. Yildirim, A. R. Vaccaro, D. J. Broer, C. W. M. Bastiaansen, A. P. H. J. Schenning, *J. Am. Chem. Soc.* **2012**, *134*, 7608; e) J. E. Stumpel, E. R. Gil, A. B. Spoelstra, C. W. M. Bastiaansen, D. J. Broer, A. P. H. J. Schenning, *Adv. Funct. Mater.* **2015**, *25*, 3314; f) G. Chen, M. Ni, H. Peng, F. Huang, Y. Liao, M. Wang, J. Zhu, V. A. L. Roy, X. Xie, *ACS Appl. Mater. Interfaces* **2017**, *9*, 1810. g) C. Altintas, I. Erucar, S. Keskin, *ACS Appl. Mater. Interfaces* **2018**, *10*, 4; h) Z. Deng, G. Zhou, L. T. Haan, *ACS Appl. Mater. Interfaces* **2019**, *11*, 36044; i) D. Myung, S. Hussain, S. Park, *Sens. Actuators, B* **2019**, *298*, 126894; j) Z. Zheng, C. Tang, J. T. W. Yeow, *Sens. Actuators, B* **2020**, *320*, 128596.

[3] a) Z. H. Zhang, J. W. Zhang, C. F. Cao, K. Y. Guo, L. Zhao, G. D. Zhang, J. F. Gao, L. C. Tang, *Chem. Eng. J.* **2020**, *386*, 123894; b) X. W. Liu, R. Wang, T. Zhang, Y. He, J. C. Tu, X. T. Li, *Sens. Actuators, B* **2010**, *150*, 442.

[4] S. Mohd-Noor, J. Hansol, K. Baek, Y. R. Pei, A. M. Alam, Y. H. Kim, I. S. Kim, J. H. Choy, J. Hyun, *J. Mater. Chem. A* **2019**, *7*, 10561.

[5] W. Hu, M. Chen, Q. Wang, L. Y. Zhang, X. T. Yuan, F. W. Chen, H. Yang, *Angew. Chem., Int. Ed.* **2019**, *58*, 6698.

[6] A. J. J. Kragt, D. J. Broer, A. P. H. J. Schenning, *Adv. Funct. Mater.* **2018**, *28*, 1704756.

[7] a) K. E. Shopsowitz, H. Qi, W. Y. Hamad, M. J. Maclachlan, *Nature* **2010**, *468*, 422; b) O. Kose, A. Tran, L. Lewis, W. Y. Hamad, M. J. MacLachlan, *Nat. Commun.* **2019**, *10*, 510; c) K. Adstedt, E. A. Popenov, K. J. Pierce, R. Xiong, R. Geryak, V. Cherpak, D. Nepal, T. J. Bunning, V. V. Tsukruk, *Adv. Funct. Mater.* **2020**, *30*, 2003597.

[8] a) B. Tardy, J. J. Richardson, L. G. G. Greca, J. L. Guo, H. Ejima, O. J. Rojas, *Adv. Mater.* **2020**, *32*, 1906886; b) M. C. Xu, X. Y. Wu, Y. Yang, C. H. Ma, W. li, H. P. Yu, Z. J. Chen, J. Li, K. Zhang, S. X. Liu, *ACS Nano* **2020**, *14*, 11130.
[9] C. Y. Sun, D. D. Zhu, H. Y. Jia, K. Lei, Z. Zheng, X. L. Wang, *ACS Appl. Mater. Interfaces* **2019**, *11*, 39192.
[10] H. H. Chen, A. Q. Hou, C. W. Zheng, J. Tang, K. L. Xie, A. Q. Gao, *ACS Appl. Mater. Interfaces* **2020**, *12*, 24505.
[11] C. Boott, A. Tran, W. Hamad, M. MacLachlan, *Angew. Chem., Int. Ed.* **2020**, *59*, 226.
[12] T. X. Chen, Q. L. Zhao, X. Meng, Y. Li, H. Peng, A. K. Whittaker, S. M. Zhu, *ACS Nano* **2020**, *14*, 9440.
[13] a) T. F. Long, Y. J. Guo, M. Lin, M. K. Yuan, Z. D. Liu, C. Z. Huang, *Nanoscale* **2016**, *8*, 9764; b) K. S. Mali, J. Adisoejoso, E. Ghijsens, I. D. Cat, S. D. Feyter, *Acc. Chem. Res.* **2012**, *45*, 1309.
[14] J. L. Shen, Q. W. Xiao, P. P. Sun, J. Feng, X. Xin, Y. Yu, W. Qi, *ACS Nano* **2021**, *15*, 4947.
[15] J. C. Liang, A. Y. Hao, P. Y. Xing, *ACS Appl. Mater. Interfaces* **2020**, *12*, 45665.
[16] X. H. Niu, X. Yang, Z. L. Mo, N. J. Liu, R. B. Guo, Z. Pan, Z. Y. Liu, *Microchim. Acta* **2019**, *186*, 557.
[17] M. Y. Gu, C. Y. Jiang, D. G. Liu, N. Prempeh, I. I. Smalyukh, *ACS Appl. Mater. Interfaces* **2016**, *8*, 32565.
[18] H. Wan, X. F. Li, L. Zhang, X. P. Li, P. F. Liu, Z. G. Jiang, Z. Z. Yu, *ACS Appl. Mater. Interfaces* **2018**, *10*, 5918.
[19] a) H. B. Qiu, J. B. Gilroy, I. V. Manners, *Chem. Commun.* **2013**, *49*, 42; b) X. L. Liu, M. G. Li, T. Han, B. Cao, Z. J. Qiu, Y. Y. Li, Q. Y. Li, Y. B. Hu, Z. Y. Liu, J. W. Y. Lam, X. L. Hu, B. Z. Tang, *J. Am. Chem. Soc.* **2019**, *142*, 11259.
[20] P. Martin, G. Vasilyev, G. Chu, M. Boas, A. Arinstein, E. Zussman, *J. Polym. Sci., Part B: Polym. Phys.* **2019**, *57*, 1527.
[21] K. E. Secrist, A. J. Nolte, *Macromolecules* **2011**, *44*, 2859.
[22] N. Joshi, K. Rawat, H. B. Bohidar, *Food Hydrocolloids* **2018**, *74*, 132.
[23] J. Grooth, R. Oborný, J. Potreck, K. Nijmeijer, W. M. Vos, *J. Membr. Sci.* **2015**, *475*, 311.
[24] S. Dickman, *Science* **1993**, *262*, 500.
[25] C. C. Y. Cheung, M. Giese, J. A. Kelly, W. Y. Hamad, M. J. MacLachlan, *ACS Macro Lett.* **2013**, *2*, 1016.
[26] M. Kengo, *Prog. Org. Coat.* **2020**, *142*, 105599.
[27] J. Z. Cao, G. J. Zhao, *Holzforschung* **2000**, *54*, 321.
[28] H. A. Resing, R. A. Neihof, *J. Colloid Interface Sci.* **1970**, *34*, 480.
[29] J. Široký, R. S. Blackburn, T. Bechtold, J. Taylor, P. White, *Carbohydr. Polym.* **2011**, *84*, 299.
[30] T. Hiratani, O. Kose, W. Y. Hamad, M. J. MacLachlan, *Mater. Horiz.* **2018**, *5*, 1076.
[31] V. D'Ambrosio, N. Spagnolo, L. D. Re, S. Slussarenko, Y. Li, L. C. Kwek, L. Marrucci, S. P. Walborn, L. Aolita, F. Sciarrino, *Nat. Commun.* **2013**, *4*, 2432.
[32] G. M. Zhao, Y. Zhang, S. C. Zhai, J. Sugiyama, M. Z. Pan, J. B. Shi, H. Y. Lu, *ACS Appl. Mater. Interfaces* **2020**, *12*, 17833.
[33] G. M. Zhao, J. Du, W. M. Chen, M. Z. Pan, D. Y. Chen, *Cellulose* **2019**, *26*, 8625.
[34] H. E. Lee, H. Y. Ahn, J. Mun, Y. Y. Lee, M. Kim, N. H. Cho, K. Chang, W. S. Kim, J. Rho, K. T. Nam, *Nature* **2018**, *556*, 360.